ACS OMEGA

Open Access

http://pubs.acs.org/journal/acsodf

Article

Photoresponse of Carbon Nanofiber-Based Photodetector and Its Enhancement on CuNi Nanoparticle Adsorption

Shivam Shukla, Subhajit Jana, Anu Gupta, Subhadip Ghosh, Samit K. Ray, and Sanjeev K. Srivastava*

Cite This: *ACS Omega* 2024, 9, 27232−27247

Read Online

ACCESS | Metrics & More | Article Recommendations | Supporting Information

ABSTRACT: We explore the photodetection properties of a carbon nanofiber (CNF)-based p-CNF/n-Si heterojunction device in the 400−800 nm wavelength range and investigate the changes brought in by adsorption of CuNi (CN) nanoparticles on the CNFs. The nanoparticles and CN-CNF nanocomposites were synthesized by using chemical hydrothermal routes. The p-type semiconducting nature of the CNFs and nanocomposites was determined using X-ray photoelectron (XPS) and UV−vis spectroscopies. The p-CNF/n-Si device is found to be better than many carbon-nanotube-based devices in terms of its peak responsivity (0.6 A/W) and gain (1.6), with an acceptably moderate peak detectivity (1.3×10^9 Jones) at 450 nm and a −5 V bias. The p-CN-CNF/n-Si device displays an appreciable enhancement in the photoresponse with respect to the p-CNF/n-Si device, with a peak responsivity of 2.8 A/W, peak detectivity of 9.4×10^9 Jones, and gain of 8. With the aid of valence band XPS and Raman spectra, the enhancement is explainable in terms of a CN to CNF charge transfer and the resulting increase in the built-in potential at the heterojunction.

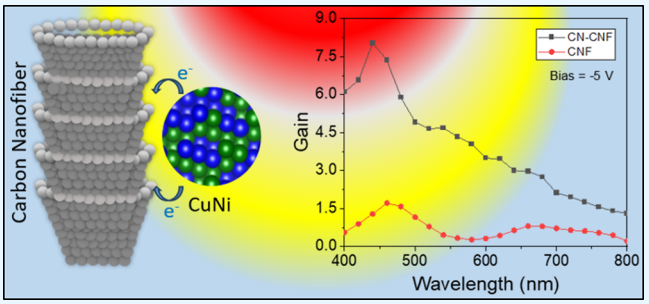

INTRODUCTION

Photodetectors are of paramount importance in various fields, like communication, security, energy harvesting, aerospace, defense, biochemical sensing, etc.[1−9] Most of the commercial photodetectors are fabricated using Si, Ge, and InGaAs.[1,10] These photodetectors are, however, costly to produce.[1] This necessitates the development of low cost, preferably high-performance, and broadband photodetectors. Carbon nanotubes (CNTs), which have adjustable band gaps and hence broadband absorption, have emerged rapidly as an essential component of photodetectors.[11−14] Photodetectors based on heterostructures of single- and multiwalled CNTs (SWCNTs and MWCNTs) and Si, Ge, SiO_2 or GaAs have been studied for photodetection in optical and near-infrared spectral ranges.[1,10,15−19] However, CNTs come with their own limitations, like moderate thermal stability and mechanical strength,[13,16,20] making it desirable to search for materials that can provide improved photodetection properties on one hand and better thermal and mechanical stability on the other. In this regard, carbon nanofibers (CNFs) could be a suitable alternative to CNTs, because, along with showing similar optical properties,[13,21] they possess a larger specific surface area that could be beneficially utilized for photocarrier generation and are cheaper and easier to produce.[13,22,23] The large active surface area and excellent conductivity of CNFs have recently been utilized by combining CNFs with biomolecules, polymers, and inorganic substances. To the best of the authors' knowledge, CNFs have hitherto not been studied for their utility in photodetection. Hence, it is intriguing to explore what kind of photodetection properties a CNF-based photodetector can have.

As per the existing literature, functionalization of CNTs with other nanostructures is known to improve the photodetection properties of CNT-based photodetectors.[16,18,24] In the cases of metal (Ag, Au, and Cu) nanoparticles (NPs), e.g., a strong plasmonic local field generated on the CNTs is reported to enhance the photocurrent.[16,18] Semiconducting TiO_2 and CdS NPs, on the other hand, enhance the photoresponse via a charge transfer to the CNT layer in contact.[24] For the semiconducting adsorbent NPs, it is reported that a photon can also be absorbed in the NP, resulting in the generation of an excited electron that subsequently gets transferred to the CNTs and adds to the photocurrent. Such a charge transfer has recently been demonstrated by our group also between $Cu_{1-x}Ni_x$ alloy NPs and a C allotrope, viz., reduced graphene oxide.[25] It is intriguing to investigate whether adhesion of these alloy NPs to CNFs produces, via charge transfer, any change in the photodetection properties of the CNF-based devices being explored.

Received: February 18, 2024
Revised: April 15, 2024
Accepted: June 7, 2024
Published: June 13, 2024

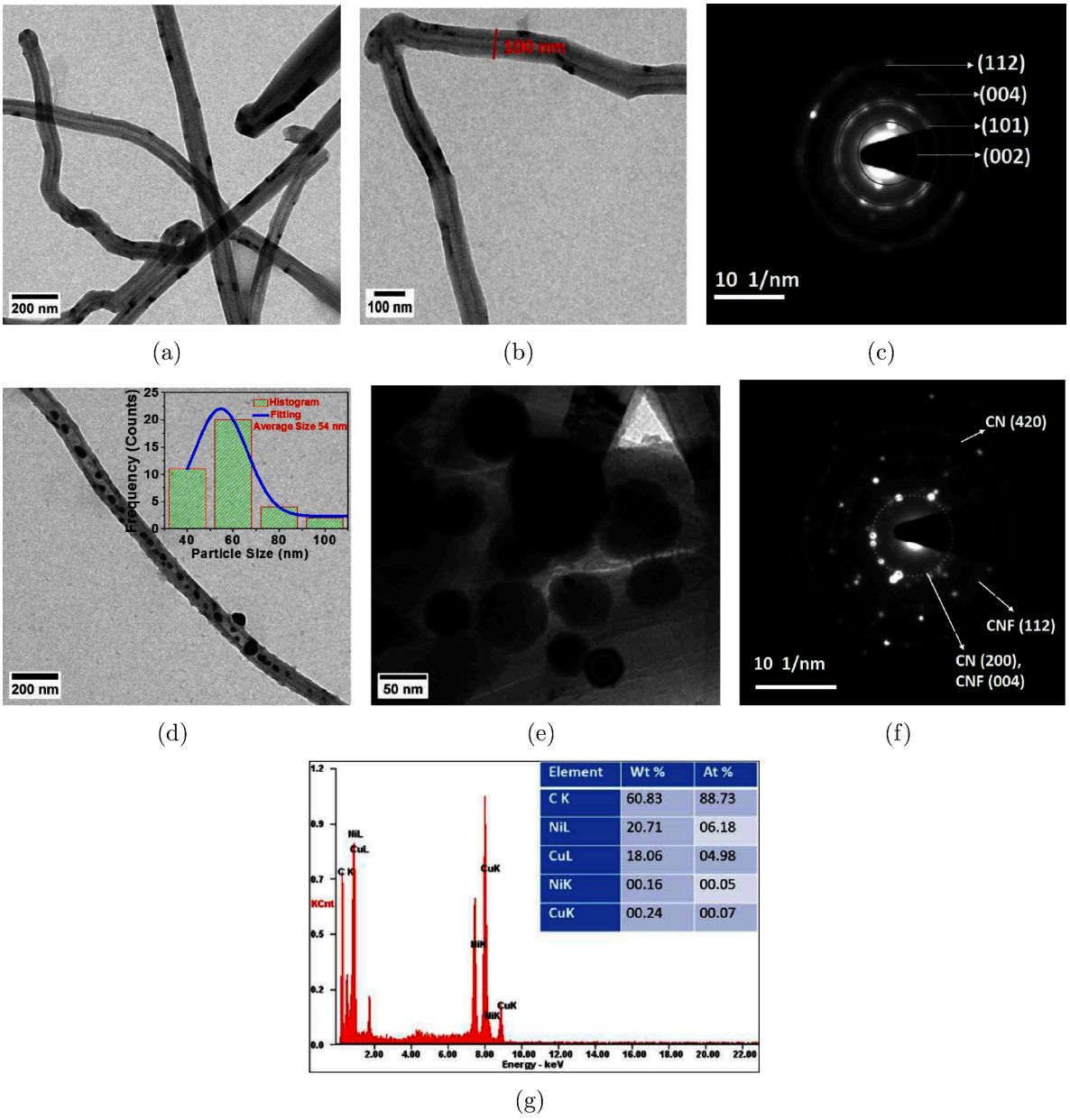

Figure 1. (a and b) TEM micrographs of CNFs at different magnifications and (c) the corresponding SAED pattern. (d and e) TEM micrographs of CNFs with CN NPs adsorbates at different magnifications. The inset in d is the particle size histogram. (f) SAED pattern of the CN-CNF sample. (g) EDX spectra of the CN-CNF sample. The inset of g displays the elemental composition.

In this work, we (i) investigate whether a hitherto unexplored C material, CNF, can show photodetection properties when in a CNF/Si heterojunction configuration and (ii) explore whether these properties can be enhanced by adhesion of CuNi (CN) NPs on CNFs. For this exploratory study, we have restricted the composition of $Cu_{1-x}Ni_x$ to x = 0.5. The CN NPs and CN-CNF nanocomposites are synthesized by using a chemical hydrothermal method. The devices are prepared by spin-coating CNFs and CN-CNF nanocomposites on n-type Si substrates and then depositing appropriate metal contacts onto the heterostructures. The CNF/Si device itself is found to exhibit photodetection properties, with a performance that is better than many CNT based devices. On the adhesion of CNs to CNF, a charge transfer from CN to CNF is inferred, which results in an increase in the built-in potential at the interface and therefore a significant enhancement in the photoresponse with respect to the CNF/Si device. The performances of the CNF/Si and CN-CNF/Si devices are found to be good enough for practical applications.

EXPERIMENTAL SECTION

Synthesis and Characterization of CN and CN-CNF Nanocomposites. For the preparation of CN and CN-CNF nanocomposites, $CuCl_2{\cdot}2H_2O$, $NiCl_2{\cdot}6H_2O$, and sodium dodecyl sulfate (SDS) powders; CNF powders composed of conical platelets; and triethanolamine, hydrazine hydrate, and dimethylformamide (DMF) liquids were purchased from Sigma-Aldrich. To synthesize CN nanoparticles, 5.13 mmol of $CuCl_2{\cdot}2H_2O$ and 4.20 mmol of $NiCl_2{\cdot}6H_2O$ were first dissolved in 10 mL of distilled water. After stirring this solution for 10 min, 5 mL of triethanolamine and 2 mL of hydrazine

https://doi.org/10.1021/acsomega.4c01546
ACS Omega 2024, 9, 27232−27247

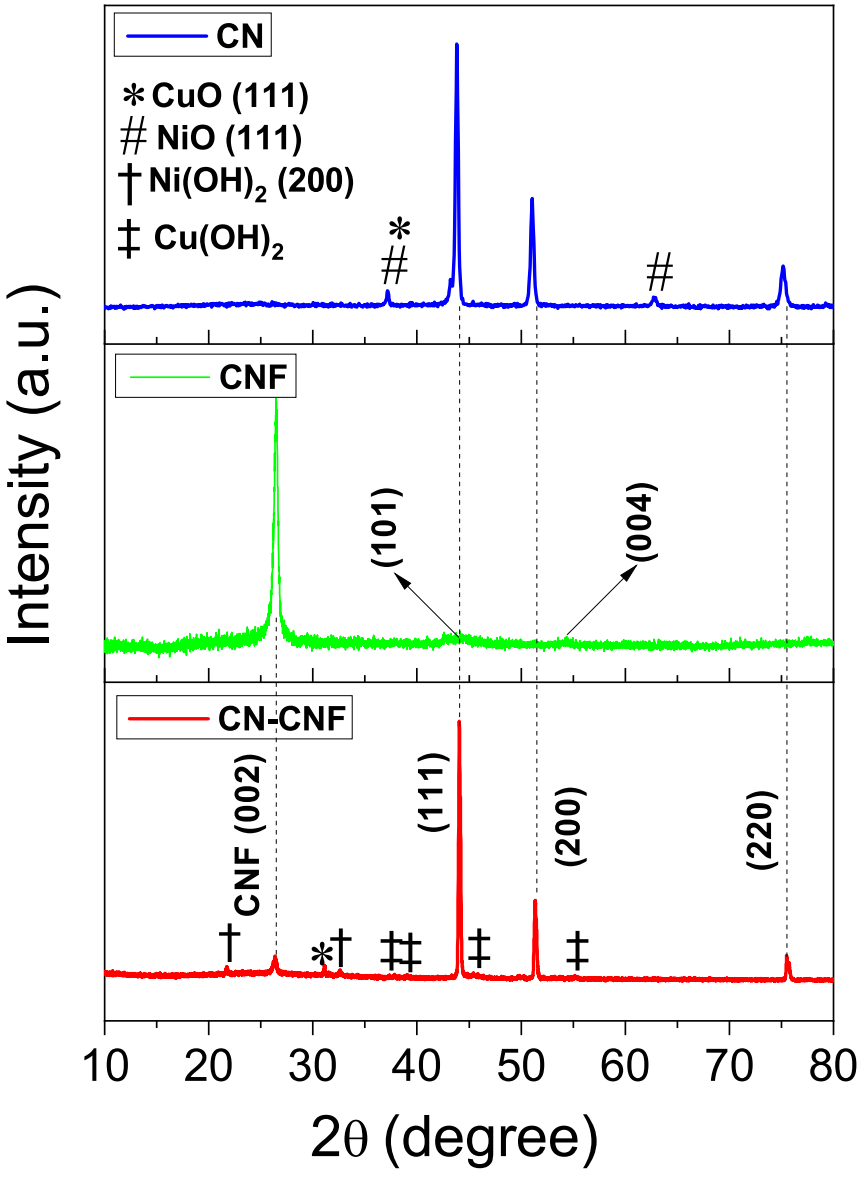

Figure 2. XRD patterns of CN NPs, CNF, and CN-CNF composites.

hydrate were added as a surfactant and reducing agent, respectively. Hydrothermal treatment of the resulting solution was performed at 150 °C for 15 h. The black-colored product formed in this process was filtered and washed several times with distilled water and ethanol and then dried in a vacuum oven for 12 h. The synthesized product was annealed in a tube furnace at 800 °C for 2 h in the presence of Ar gas. The only difference in preparing the CNF decorated (CN-CNF) samples was that $CuCl_2{\cdot}2H_2O$ and $NiCl_2{\cdot}6H_2O$ were dissolved in a CNF and SDS (CNF-SDS) solution instead of water.

Finally, the CNF and CN-CNF powders were dissolved in DMF, and the solutions were kept for device preparation. The structural and morphological characteristics of CNFs and CN-CNF nanocomposites were studied by an analytical transmission electron microscope (TEM) using a JEOL JEM-2100 microscope at an operating voltage of 200 kV. The microscope was also used to record selected area electron diffraction (SAED) patterns from the samples. The TEM was additionally used to record the energy dispersive analysis of X-ray (EDX) spectra of the CN-CNF sample to determine the quantitative loading of CN NPs. The EDX spectrum was recorded by scanning a 200 × 200 nm^2 area. For determining the crystal structure and chemical states, X-ray diffraction (XRD) and X-ray photoelectron spectroscopy (XPS) measurements were performed using a Bruker D2 phaser second generation diffractometer and a PHI5000 Versaprobe X-ray photoelectron spectrometer, respectively. Raman spectra were taken using a LabRam HR evolution Horiba spectrometer. UV−vis absorption spectroscopy was performed on the samples using a PerkinElmer Lambda 2 spectrometer in the wavelength range 300−1100 nm.

Device Fabrication and Characterization. For the fabrication of heterostructure CNF/n-Si (CN-CNF/n-Si), the CNF (CN-CNF) solution was spin coated onto a 1 cm × 1 cm n-Si substrate at 1500 rpm for 200 s. Thin Al film on the back side and multiple 2 mm^2 Au contacts on the coated side were deposited by thermal evaporation. For each case, low-statistics $I-V$ measurements were performed on four devices. The four $I-V$ curves were found to be similar. The device with the best phototo-dark current ratio was chosen for

https://doi.org/10.1021/acsomega.4c01546
ACS Omega 2024, 9, 27232−27247

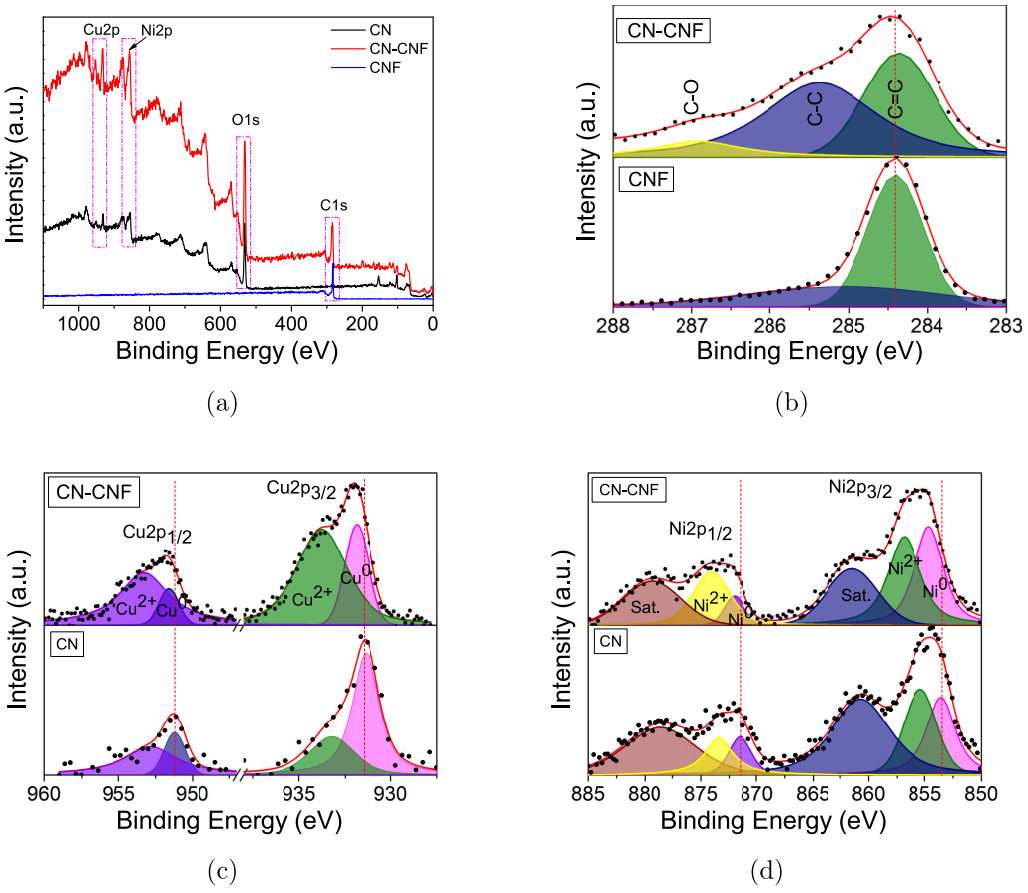

Figure 3. (a) Survey XPS spectrum of CNFs, CN NPs, and CN-CNF nanocomposites. (b) High-resolution C 1s XPS spectra, deconvolutions, and peak assignments for CNFs and CN-CNF nanocomposites. High-resolution XPS spectra, deconvolutions, and peak assignments for CN NPs and CN-CNF nanocomposites in Cu 2p (c) and Ni 2p (d) regions.

further study. Cross-sectional field emission scanning electron microscopy (FESEM) images of the devices were recorded using a ZEISS MERLIN microscope. Optical responses of the devices were measured in the laboratory under ambient conditions using a broadband light source, a monochromator, and a Keithley semiconductor parameter analyzer (4200A-SCS). A 325 nm laser was also used to measure the current−voltage (I−V) and current−time (I−t) characteristics of the devices. Between the measurements, the devices were stored in a vacuum to avoid environmental degradation.

RESULTS AND DISCUSSION

The TEM images of CNFs at different magnifications are shown in Figure 1a,b. The images reveal that the CNFs are cylindrical in shape, with a diameter of around 100 nm and a length exceeding several micrometers. The SAED pattern of CNF, as shown in Figure 1c, is composed of rings and some bright spots. This verifies the polycrystalline nature of the cone−platelet stacked CNFs. The rings are indexable as (002), (101), (004), and (112) planes of CNF, according to a report by Wei et al.[26] Figure 1d,e show the TEM micrographs of the CN-CNF sample at different magnifications. The figures suggest that multiple-sized, nearly spherical particles are sprayed all along the outer surface of the CNF. The inset of Figure 1d displays the size distribution of the particles. According to the inset, the particle size ranges from 40 to 100 nm, with a mean diameter of 54 nm. These nanosized particles ought to be the CN NPs. The SAED pattern of the CN-CNF sample is shown in Figure 1f. The pattern displays bright spots, many of which are arranged tentatively around three circles, as drawn with dotted lines in the figure. This suggests that even this sample is polycrystalline in nature. The spots around the innermost circle are likely to come either from the (004) planes of CNF[26] or from the (200) planes of CN. The middle circle can be indexed as CNF (112).[26] The outermost circle, finally, can be indexed as CN (420) from JCPDS cards 04-0836 and 04-0850. The rest of the scattered bright spots may be considered to arise from the CN NPs. Thus, the TEM images and the SAED pattern of the CN-CNF sample together verify that the CN particles indeed decorated the CNFs on their surface. The EDX spectrum of the CN-CNF sample is displayed in Figure 1g, the inset of which shows the elemental composition. As determined by EDX analysis, the CuNi NPs are 10% of the CN-CNF composite.

The XRD patterns of the CN alloy nanoparticles, CNFs, and CN-CNF nanocomposites are shown in Figure 2. The XRD pattern of CN exhibits three prominent peaks at 43.8°, 51.0°, and 75.0°. These peaks lie between the (111), (200), and (220) planes of Cu (43.6°, 50.8°, and 74.4° according to JCPDS card number 04-0836) and Ni (44.5°, 51.9°, and 76.4° according to JCPDS card number 04-0850). This suggests that the CN sample is a proper alloy of Cu and Ni. There is a very small peak at 37.1°, which can be assigned to either CuO (111)[27] or NiO (111),[28] and another at 62.7°, assignable to NiO (111).[28] This means that the sample contains these

https://doi.org/10.1021/acsomega.4c01546
ACS Omega 2024, 9, 27232−27247

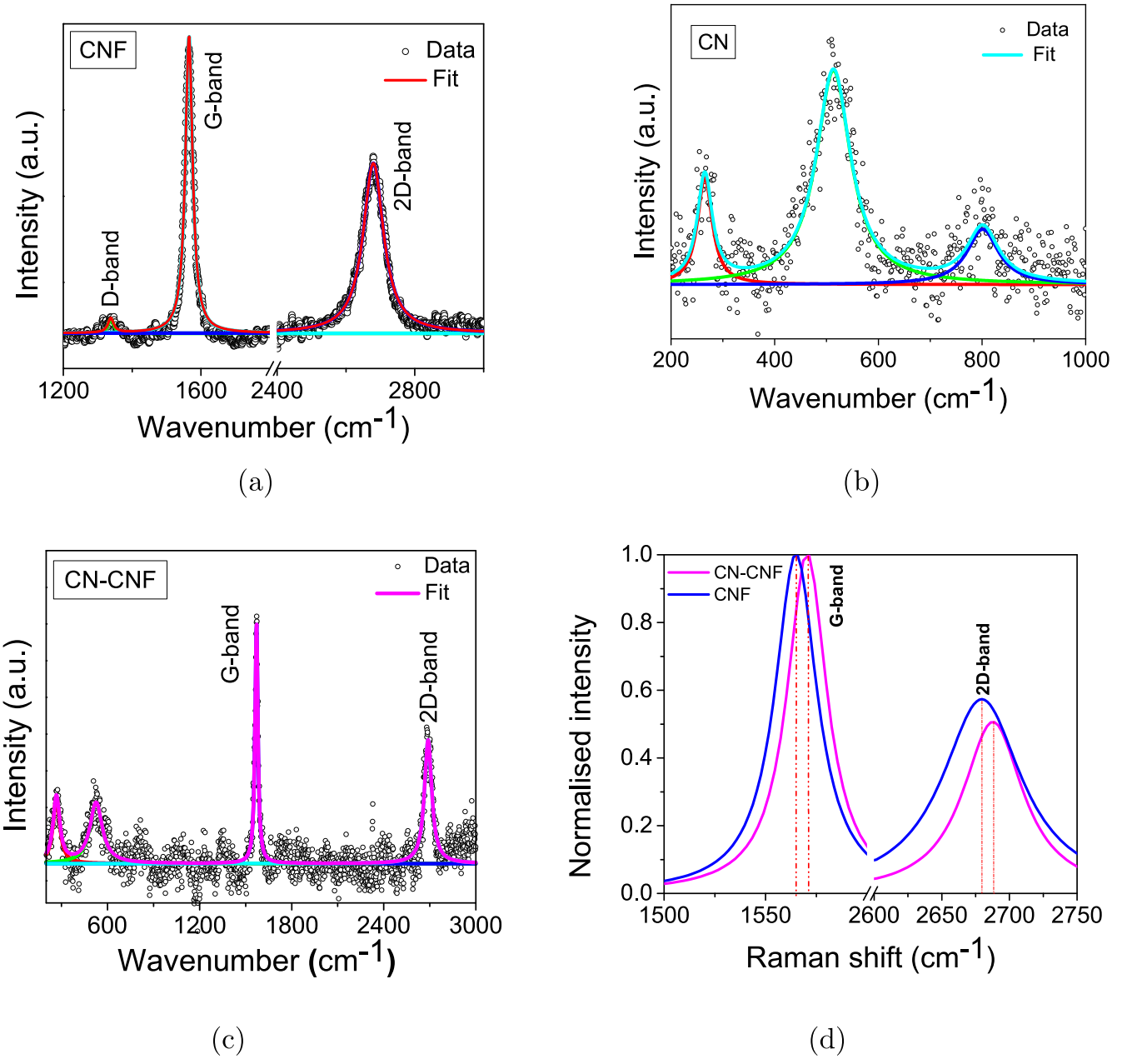

Figure 4. Raman spectra with peak fits for (a) CNFs, (b) CN NPs, and (c) CN-CNF composites. (d) A comparison between the CNF and CN-CNF Raman spectra showing the peak shifts.

oxides but with amounts so negligible that they would affect the results to any considerable extent.

The XRD pattern of the CNF samples has a prominent peak at 26.2°, along with two tiny peaks at 43.9° and 54.4°. These peaks are indexed as (002), (101), and (004) planes, respectively, which correspond to the hexagonal graphite structure of CNF.[29,30]

For the CN-CNF sample, all of the peaks corresponding to both CN and CNF are present in the pattern, suggesting that the CNFs have indeed been decorated with the CN NPs. However, the intensity of the CNF (002) peak is very small. The reason for the small C peak, even when the CN loading is only 10%, lies in the atomic form factors for X-ray scattering. The atomic form factors of Cu (~24 $Å^{-1}$) and Ni (~22 $Å^{-1}$) in the 2θ range where the peaks occur is at least an order of magnitude higher than the atomic form factor of C (~3.5 $Å^{-1}$), as determined using a calculator available on a Web page.[31] This leads to an order of magnitude smaller intensity of the C peak than expected from merely considering the atomic fractions.

Furthermore, the presence of several tiny peaks at 21.7°, 31.1°, 32.6°, 37.8°, 39.2°, 45.5°, and 55.2° can be attributed to $Ni(OH)_2$ (001),[32] CuO (110),[27] $Ni(OH)_2$ (200),[32] $Cu(OH)_2$ (041), $Cu(OH)_2$ (130), $Cu(OH)_2$ (112), and $Cu(OH)_2$ (061),[33] respectively. These peaks indicate that the oxides and hydroxides present in this sample are negligible.

XPS spectra of the three samples (CN, CNF, and CN-CNF) were taken to find the chemical states of the elements present and any possible charge transfer. Figure 3a displays the survey XPS spectra of all three samples. The spectra have been corrected to the adventitious C 1s peak at 284.4 eV. The presence of a C peak in CNF; O, Cu, and Ni in CN; and C, O,

https://doi.org/10.1021/acsomega.4c01546
ACS Omega 2024, 9, 27232−27247

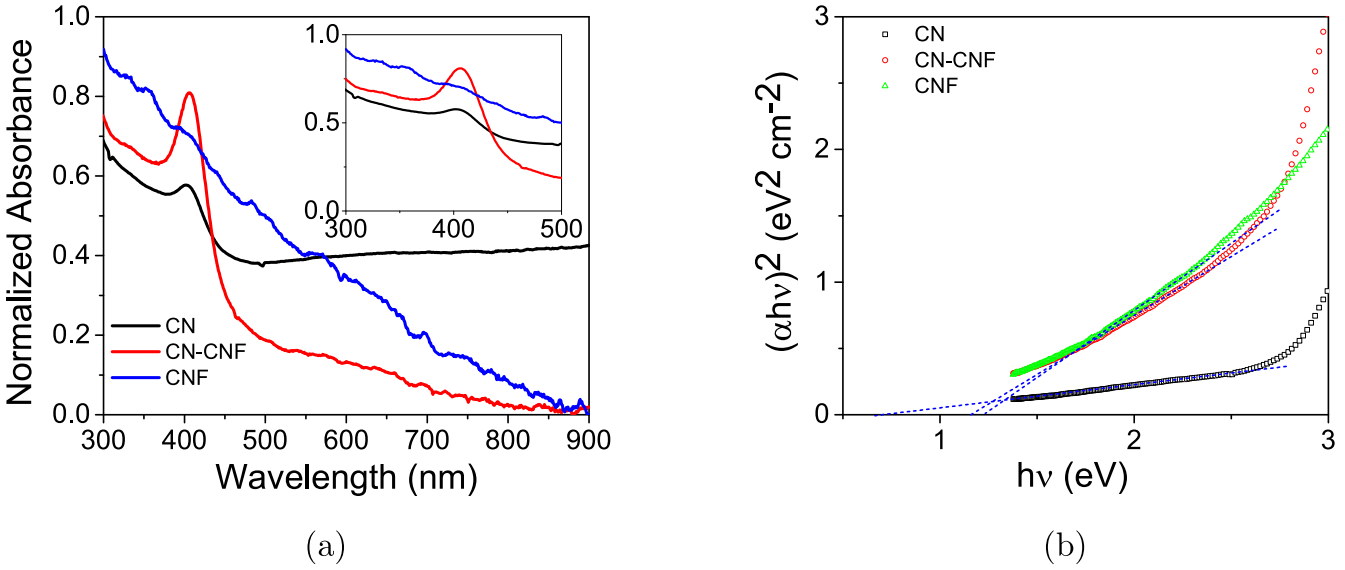

Figure 5. (a) Normalized UV−visible absorption spectra of CN NPs, CN-CNF composites, and bare CNFs. The inset shows an enlarged view of the spectra. (b) Tauc plots for the CN, CN-CNF, and CNF samples. The dotted lines are to indicate the band gaps.

Cu, and Ni in CN-CNF spectra imply that the samples are prepared as intended. Figure 3b shows a comparison between the C 1s-region high-resolution spectra (with their deconvolutions and peak identifications) of the CNF and CN-CNF samples. The *y* axis of the CN-CNF spectrum is multiplied 3.4 times for visual clarity. The CNF C 1s spectrum consists of a peak at a binding energy (BE) of 284.39 eV, corresponding to sp^2 C (C═C), and another peak at 285.14 eV that can be assigned to sp^3 C (C−C). These peaks are expected in CNFs.[34,35] These peaks occur also for the CN-CNF sample but at slightly lower BEs: C═C at 284.35 eV and C−C at 285.47 eV. This shift (with respect to the C 1s spectrum of CNF) of roughly −0.05 eV is indicative of a transfer of electrons (charge) from the CN NPs to CNFs. Shifts of this magnitude are reported earlier for charge transfer among different elements of a multicomponent alloy.[36] If this negative shift is due to a charge transfer from CNFs to CN NPs, it should be accompanied by positive BE shifts in the 2p-region high-resolution Cu and Ni spectra of the CN-CNF sample with respect to the CN NPs.[37] The CN-CNF C 1s spectrum consists of an additional weak, broad peak at around 287.0 eV that can be assigned to a C−O bond.[35] A thin layer (accessible with XPS) on the surface of the CN NPs is likely to have oxidized and brings in the observed O component in the CN-CNF C 1s spectrum.

The Cu 2p-region high-resolution XPS spectra, their deconvolutions, and the peak assignments for the CN and CN-CNF samples are shown in Figure 3c. For the CN sample, the Cu $2p_{3/2}$ subregion consists of a peak at 931.37 eV, corresponding to metallic Cu (Cu^0), and another peak at 933.25 eV assignable to CuO (Cu^{2+}); the corresponding $2p_{1/2}$ peaks occur at 951.12 and 953.00 eV.[34] The presence of the CuO peak is in line with the XRD results. For the CN-CNF sample, these peaks are still present but are shifted by roughly +0.5 to 931.80 and 933.82 eV in the $2p_{3/2}$ subregion and 951.57 and 953.32 eV in the $2p_{1/2}$ subregion. The Ni 2p-region high-resolution spectra for the two samples are shown in Figure 3d, together with their deconvolutions and peak assignments. The Ni $2p_{3/2}$ subregion is composed of a metallic Ni (Ni^0) peak at 853.55 eV and a $Ni(OH)_2$ (Ni^{2+}) peak at 855.42 eV; the corresponding peaks in the $2p_{1/2}$ subregion occur at 17.3 eV higher BEs.[34,38] The spectra also contain satellite peaks in both the subregions. The presence of the $Ni(OH)_2$ peak is justifiable from the XRD results. The corresponding CN-CNF peaks are shifted by +0.9 eV with respect to CN. The simultaneous negative BE shift in the C 1s spectrum and positive BE shifts in the Cu and Ni spectra confirm that electron (charge) transfer has taken place from both of the elements Cu and Ni of the NPs to the C atoms in CNFs on blending the NPs with CNFs.[37]

The occurrence of charge transfer, as inferred from the XPS results, can be further strengthened if the same can be deduced from another complementary technique. Raman spectroscopy is one such technique that has been used to investigate any charge transfer between a C allotrope and a substance in contact[25] and, so, has been performed on the CNF, CN, and CN-CNF samples. The Raman spectrum of the CNF sample and the peak fittings are shown in Figure 4a. A typical Raman spectrum of C based materials features a characteristic peak at ∼1590 cm^{-1} (G-band) and another at ∼1350 cm^{-1} (D-band) in case there are defects as well. The G band arises from the E_{2g} mode vibrations associated with in-plane stretching of the C−C bonds, while the D band has its origin in the A_{1g} mode breathing associated with basal plane defects in the C−C network.[25,39,40] The CNF spectrum, accordingly, contains a small D-band peak at 1338 cm^{-1} and a G-band peak at 1564 cm^{-1}. The spectrum also has another, larger defect peak—the 2D peak[25]—at 2680 cm^{-1}. 2D peaks larger than the associated D peaks are reported earlier for C-based materials, like graphene.[41] The Raman spectrum of the CN NPs, along with the peak fits, is shown in Figure 4b.

The spectrum comprises three distinct peaks. The initial peak observed at 280 cm^{-1} can be attributed to the A_g mode of CuO.[42] The subsequent peak at 540 cm^{-1} can be attributed to the 1P mode of NiO,[43] and the third peak at 801.4 cm^{-1} is likely to originate from $Cu(OH)_2$.[41] The presence of these oxide peaks is in accordance with the XRD and XPS results. Figure 4c displays the deconvoluted Raman spectra of the CN-CNF composite sample. Excluding the carbon D peak, which is too small to be identified from the noise in the data, the

https://doi.org/10.1021/acsomega.4c01546
ACS Omega 2024, 9, 27232−27247

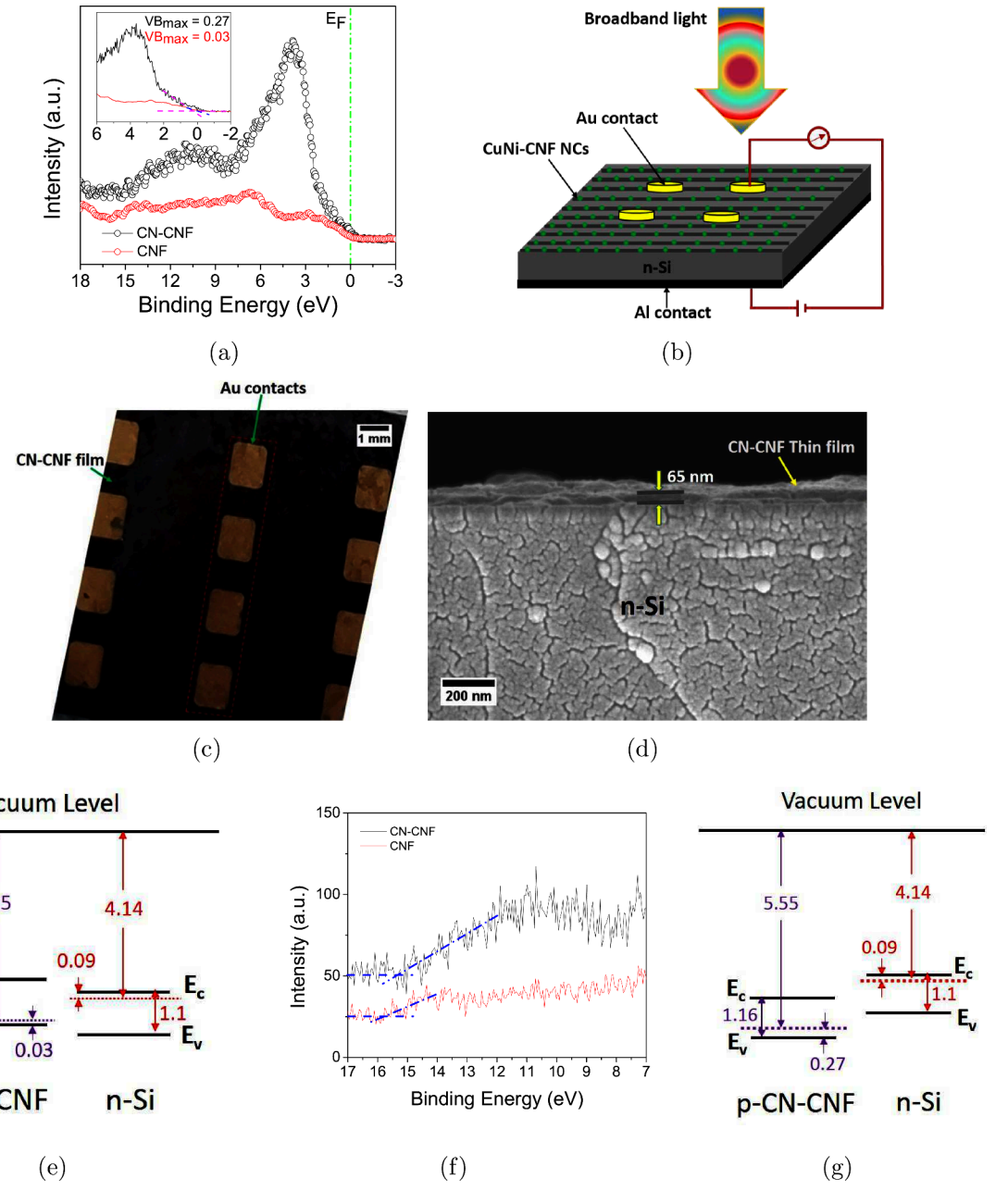

Figure 6. (a) VBXPS spectra of the CNF and CN-CNF samples. The inset highlights the positions of valence band maxima with respect to the Fermi level. (b) A schematic representation of the fabricated CNF/Si and CN-CNF/Si devices. (c) An optical photograph of the top of the device. (d) Cross-sectional FESEM image of the CN-CNF/Si device. (e) Energy level diagram for p-CNF and n-Si. (f) The VBXPS spectra in the high binding energy region highlighting the binding energies where the spectra flatten out. (g) Energy level diagram for p-CN-CNF and n-Si.

spectrum consists of all of the (five) CNF and CN peaks at nearby positions and hence asserts that the CN NPs have successfully decorated the CNFs in the CN-CNF sample.

A comparison of the positions of the G and 2D peaks for the CN and CN-CFN samples is shown in Figure 4d. After the adhesion of CN NPs, the G peak blue-shifts by 5.4 cm^{-1}, while the 2D peak blue-shifts by 8.2 cm^{-1}. The dissimilarity between the extents of the shifts ensures that it is not a rigid shift of the whole Raman spectrum and that the blue-shifts are genuine. It is known that adsorption or contact of electron donating and accepting molecules, clusters, NPs, and overlayers causes a shift in the carbon Raman peak frequencies by an amount proportional to the number of carriers injected, essentially through orbital hybridization.[37,44,45] The requirement of matching the Fermi levels of the C structure and the adsorbate leads to a transfer of charge (electron) across the interface.[46] A red (blue) shift signifies a softening (stiffening) of the Raman band arising due to charge transfer from (to) the adsorbate to (from) the C structure.[37] The blue shifts observed in Figure 4d thus are suggestive of the occurrence of charge transfer from the CN NPs to the CNFs, in perfect agreement with the inference derived from the XPS results. The direction of this charge transfer is in consonance with the principle based on electronegativities of the atomic species in contact in the following manner: A relatively more electronegative atom or functional group has a tendency to attract electrons toward itself.[47] The electronegativity of either of the adsorbate atoms Cu and Ni here is ∼1.90, while it is 2.55 for C atoms.[48] Based

https://doi.org/10.1021/acsomega.4c01546
ACS Omega 2024, 9, 27232−27247

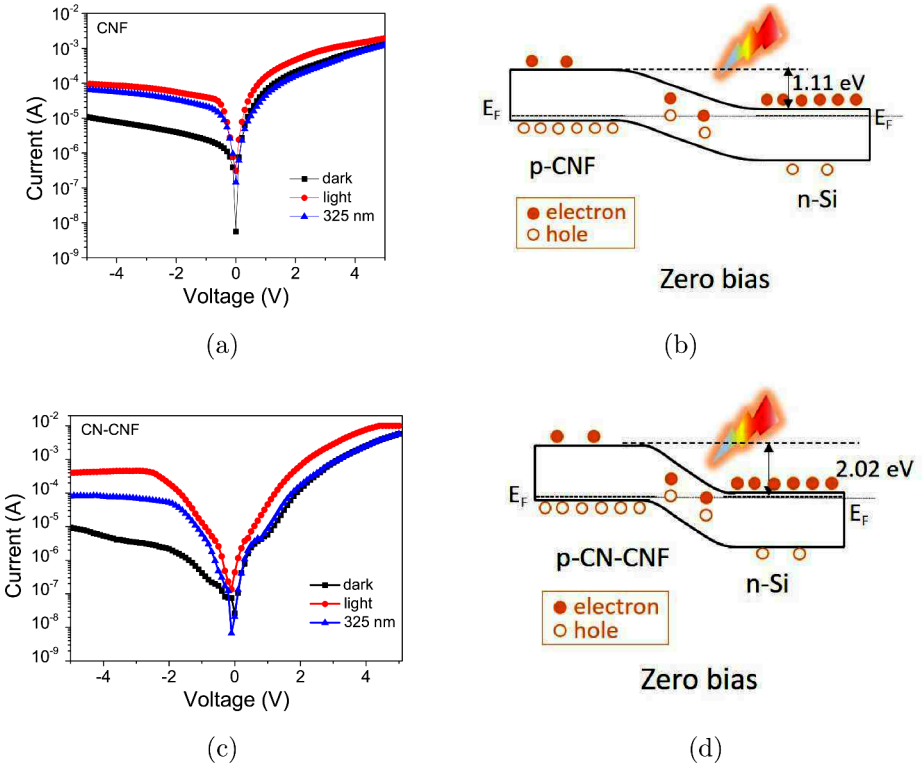

Figure 7. (a) $I-V$ characteristics (b) and zero-bias band diagram of the CNF/Si device. (c) $I-V$ characteristics (d) and zero-bias band diagram of the CN-CNF/Si device.

on this simple principle, the CNFs would have the tendency to pull electrons from the CN NPs, which will lead to a (negative) charge transfer from the CN NPs to the CNFs.

With the objective of exploring the photodetection properties, it is imperative to investigate also the optical properties, of the materials under study. Therefore, UV−vis absorption spectra of the CNFs, CN NPs, and CN-CNF composites have also been taken. The spectra between 300 and 900 nm wavelengths are shown in Figure 5a. The absorption spectrum of the CNF sample is featureless in the measured wavelength range. This is possible because the UV−vis spectra of the nearest materials SWCNT and MWCNT have also been shown not to possess any peak in this wavelength range.[49] In the case of CN NPs, a single absorption peak is observed around 400 nm, which lies roughly in the middle of the reported absorption peak of Cu NPs at around 540 nm, and that of Ni NPs at around 315 nm.[50,51] This further verifies the formation of bimetallic CN alloy NPs.[52] The CN NP absorption peak is present also in the absorption spectrum of the CN-CNF sample almost at the same position, as can be seen in the inset of Figure 5a. This once again asserts that the CN NPs have been blended with CNFs in the CN-CNF sample. The Tauc plots[53] derived from the absorption spectra are shown in Figure 5b. The plots are used to calculate band gaps by linearly fitting the initial rise of the curves and interpolating the linear fit to the wavelength axis. The line corresponding to the metallic CN NPs just misses touching the origin, perhaps because of the insulating CuO and NiO components. The band gap of CNF is 1.23 eV, suggesting that the sample is semiconducting and hence is usable as a photodetector. A band gap of this order has been reported previously for CNFs.[54] The band gap of the CN-CNF sample is slightly smaller (1.16 eV), likely due to the presence of metallic CN NPs with the semiconducting CNFs. Thus, the CN-CNF sample also can be used for photodetection studies.

The final task before making a photodetector from CNFs and the CN-CNF sample is to check whether these semiconductors are p-type or n-type. This was done by recording and analyzing valence band XPS (VBXPS) spectra. The VBXPS spectra of the two samples are shown in Figure 6a. The valence band maximum (VBM) for each sample was taken as the intersection point of the tangents, as shown in the inset of Figure 6a. The VBM of the CNF sample is located 0.03 eV below the Fermi level (E_F), while that of the CN-CNF sample is 0.27 eV below E_F. Considering the band gaps (1.23 and 1.16 eV) for these samples as determined earlier, E_F is very close to the VBM in both cases. This implies that both the CNF and CN-CNF samples are p-type semiconductors and suggests that an n-type semiconducting substrate would be appropriate for fabricating the desired devices. This is the reason why thin CNF and CN-CNF layers are deposited onto n-Si substrates for device fabrication. Figure 6b is a representative schematic of the fabricated CNF/Si and CN-CNF/Si heterostructure devices, as described in the Experimental Section. Figure 6c shows an optical photograph of the top of the CN-CNF/Si device. A cross-sectional FESEM image of the CN-CNF/Si device, taken to represent both devices as they are prepared in the same manner, is shown in Figure 6d. From the figure, the thickness of the CN-CNF film can be determined as 65 nm. The structure under each Au contact is a photodetector device. The area of ∼2 mm^2 of the Au contacts is also the active area of the device. Energy levels of the adjacent p-CNF and n-Si layers in the fabricated device can be drawn based on literature values of the band gaps and work functions (ϕ).[1,54,55] The energy level diagram is shown in Figure 6e. Since the extrema of the valence and conduction bands occur in different layers,

https://doi.org/10.1021/acsomega.4c01546
ACS Omega 2024, 9, 27232−27247

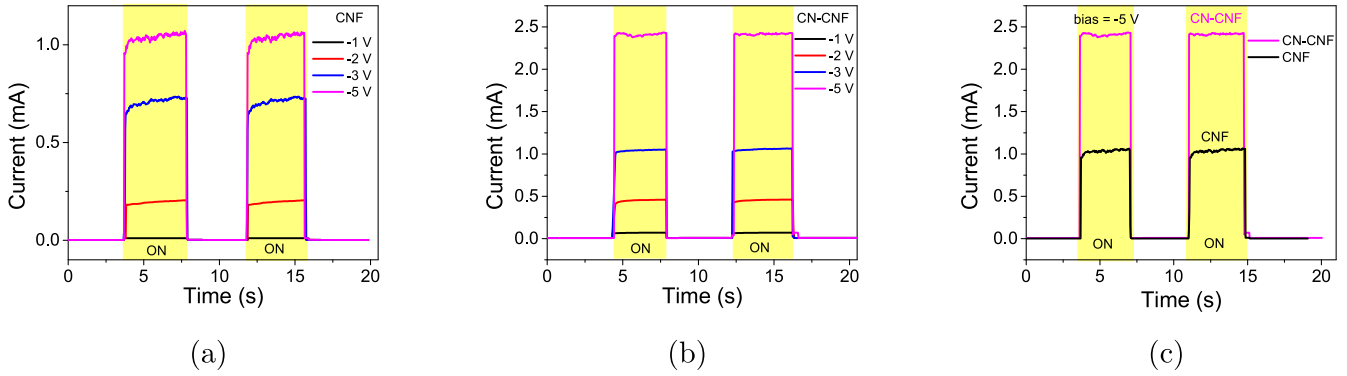

Figure 8. Bias-dependent switching characteristics of (a) CNF/Si and (b) CN-CNF/Si devices. (c) A comparison between the switching properties of the CNF/Si and CN-CNF/Si devices at −5 V bias.

this will lead to the formation of a type II heterojunction.[56] In type II heterojunctions, the built-in electric fields are known to separate carriers efficiently, resulting in enhanced photocurrents and delayed carrier recombination.[57] The changes in the energy levels caused by the adsorption of CN on CNF can be determined by noting the binding energy (BE_F) at which the VBXPS spectrum flattens on the high binding energy side.[58] The high binding energy side of the VBXPS spectra for the two samples is shown in Figure 6f, where the BE_F's are marked with crossings of linear fits to the spectra. The BE_F values for the CNF and CN-CNF samples are 15.8 and 15.2 eV, respectively. The smaller BE_F value for the CN-CNF sample suggests that its ϕ is larger by 0.6 eV than that of the CNF sample.[58] This ϕ enhancement is in agreement with the report by Qi et al.,[19] where the work function of CNTs increases on decorating them with Au NPs. Changes in the work function of a surface are caused essentially by any charge transfer to (or from) an adsorbate, and the associated surface dipole.[59−63] In general, the sign of the change depends on the relative electronegativity of the adsorbate: the work function decreases when the adsorbate is less electronegative and vice versa.[59,63] This way, since the (common) electronegativity of the adsorbate atoms Cu and Ni is less than that of the C atoms on the CNF surface, the CNF work function should decrease. However, it is also reported that the signs of the work function changes are not always determined by the electronegativity rule, i.e., by the direction of the charge transfer, and the opposite may happen.[61,63] So, the observed increase in the CNF work function on CN NP adsorption is justifiably relatable to the observed charge transfer. The energy levels as modified on the adsorption of CN on CNF are shown in Figure 6g.

Current−voltage ($I-V$) characteristics of the devices were recorded at room temperature under dark white light illumination and 325 nm UV laser illumination. The $I-V$ curves of the p-CNF/n-Si device are shown in Figure 7a. The rectifying behavior in each case can be understood from the corresponding band diagrams derived from Figure 6d,f.[64] The band diagram of the p-CNF/n-Si device under zero bias conditions is shown in Figure 7b. The built-in potential (V_{bi}) of 1.11 eV prevents the carriers on either side of the depletion region from flowing, resulting in an ideally zero current. On illumination by visible or laser light, additional carriers are generated in the depletion region. These carriers recombine in the depletion region itself in the absence of a bias, leading once again to a negligible current. In forward bias, the depletion region shortens and V_{bi} decreases, resulting in a forward current typical of a p−n junction diode. The flow of the additional carriers generated in the depletion region on illumination then enhances the forward current further. In reverse bias, the depletion region widens, and V_{bi} increases. This makes the depletion region highly resistive, preventing the current flow. However, a relatively large dark current (I_d) of 5.6×10^{-6} A at −3 V flows due to the leakage of the minority carriers. This large dark current is likely to be due to nonuniformity of the CNF film and an imperfect CNF/Si interface.[65] Similar dark currents are reported for a CNT/ZnO nanowire/p-Si device by Shao et al.[66] The additional carriers generated in the depletion region on illumination are swept away additionally, increasing the reverse current further. The photo-to-dark current ratio of the device is 13 at −3 V. This can be considered a moderate value. By fitting the dark $I-V$ curve with the standard diode equation,[58] the ideality factor η is estimated to be 5.2. The device also has a similar photoresponse under 325 nm UV illumination. The $I-V$ curves of the p-CN-CNF/n-Si device are shown in Figure 7c. As can be seen, the photoresponse of this device is enhanced significantly with respect to the CNF/Si device: the dark current is reduced to 3.0×10^{-6} A (nearly half) at −3 V, and the photo-to-dark current ratio is improved significantly to 157 (nearly 12 times) at −3 V. This improvement on the adsorption of CN NPs on CNF can be understood with the help of the corresponding band diagram shown in Figure 7d. The enhancement in V_{bi} delays the carrier recombination, which, in turn, magnifies the carrier separation efficiency and results in an increased photocurrent in all of the scenarios. However, η degrades slightly to increase to 5.5. The higher value of η with respect to the bare CNF/Si device can be ascribed to the possible enhancement in structural disorder and interfacial defects[58] arising due to the adhesion of the CN NPs.

The dynamic (switching) photoresponses of the CNF/Si and CN-CNF/Si devices under different applied biases and using white light are shown in Figure 8a and b, respectively. In accordance with Figure 7a and c, the photocurrent increases with increasing bias for both devices, and the photocurrent from the CN-CNF/Si device is enhanced compared to the CNF device at all of the bias voltages. Figure 8c, a figure derived from Figure 8a and b that shows a comparison between the switching behaviors of the two devices at −5 V bias, clearly marks the photocurrent enhancement from 1.0 to 2.4 mA on the adhesion of CN NPs on CNFs. Such a

https://doi.org/10.1021/acsomega.4c01546
ACS Omega 2024, 9, 27232−27247

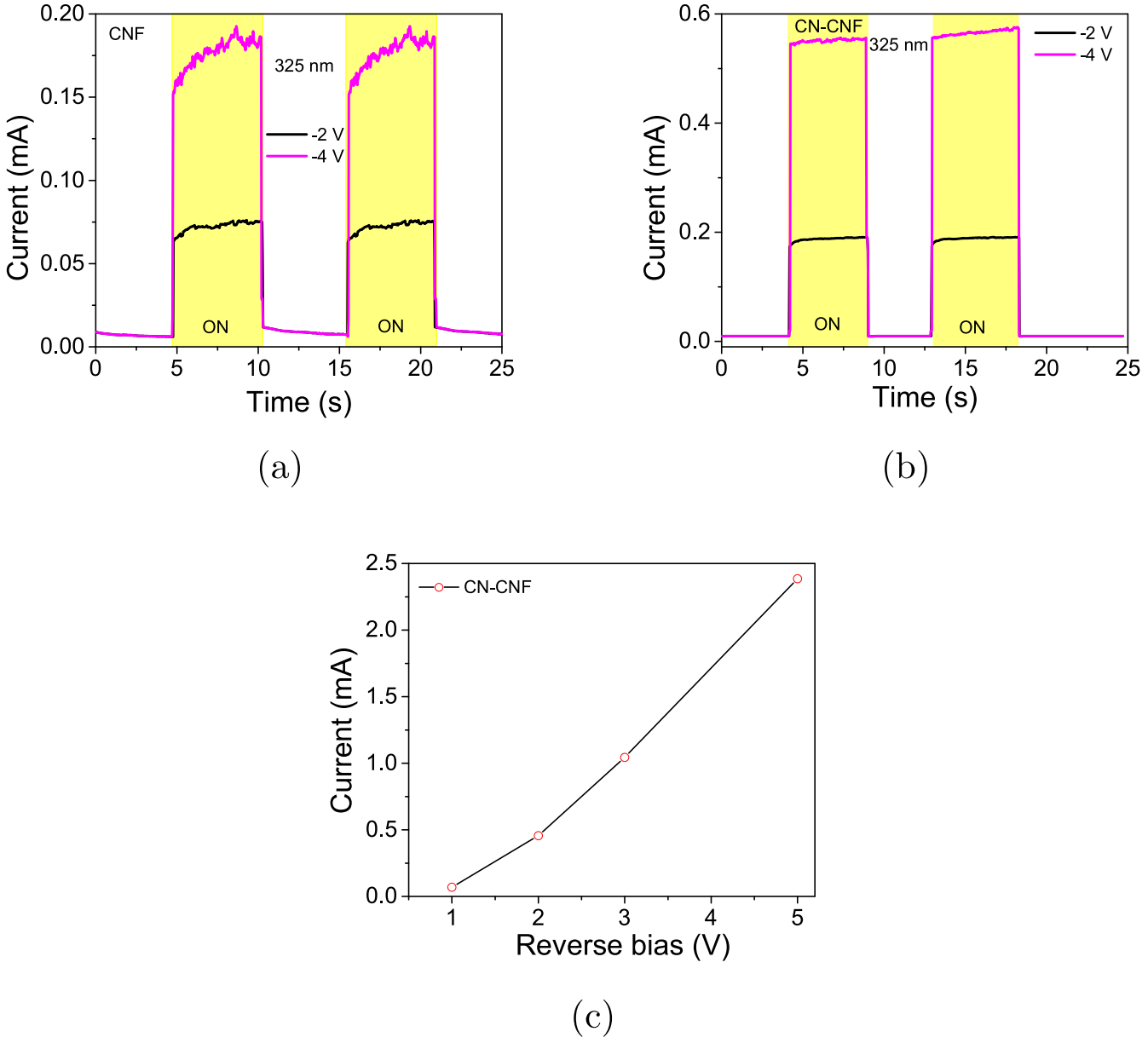

Figure 9. Bias-dependent switching characteristics of (a) CNF/Si and (b) CN-CNF/Si devices under 325 nm laser illumination. (c) Variation of photocurrent with reverse bias for the CN-CNF device.

photoresponse enhancement is also reported for CNT-based devices that were modified with cesium tungsten bronze nanoclusters.[10] Further, the photoresponses of the CNF/Si and CN-CNF/Si devices under monochromatic (325 nm) UV excitation are presented in Figure 9a and b, respectively. Qualitatively similar behaviors, as with the white light, are observable: (i) The photocurrent for each device increases on increasing bias; the plot between photocurrent and bias voltage for the CN-CNF device, as plotted in Figure 9c, illustrates this clearly. (ii) The photocurrent is ∼2.5 times higher for the CN-CNF/Si device than for the CNF/Si device.

The response (τ_r) and decay (τ_d) times constitute another set of crucial parameters of a photodetector that determines the switching speed. These times can be defined as the time interval for the photocurrent to change respectively from 10% to 90% and vice versa when the light is turned on and off. Figure 10a and b demonstrate how these values are determined for CNF/Si and CN-CNF/Si devices, respectively, under white light. The estimated τ_r and τ_d values for the CNF/Si device are 200 and 220 ms, respectively. These values are significantly better than those of the previously reported Cu−Ni alloy nanoparticle-decorated graphene-based photodetectors[67] and are comparable with switching speeds reported in the literature.[10] The estimated τ_r and τ_d values for the CN-CNF/Si device are, on the other hand, 220 and 60 ms, respectively. This means, although the rise time remains almost similar on the adhesion of CN NPs on CNFs, the decay time shortens (improves) by a factor of ∼4. Thus, the CN-CNF/Si device has switching properties much better than those of the CNF/Si device. As the CN-CNF/Si device has a larger built-in potential and hence a larger electric field across the depletion region, the photogenerated carriers are more quickly swept away on removal of the light, leading to a shorter decay time.[19]

There are three key figures of merit of a photodetector:[58,68] (i) the responsivity R, a measure of the sensitivity of the photodetector and given by

https://doi.org/10.1021/acsomega.4c01546
ACS Omega 2024, 9, 27232−27247

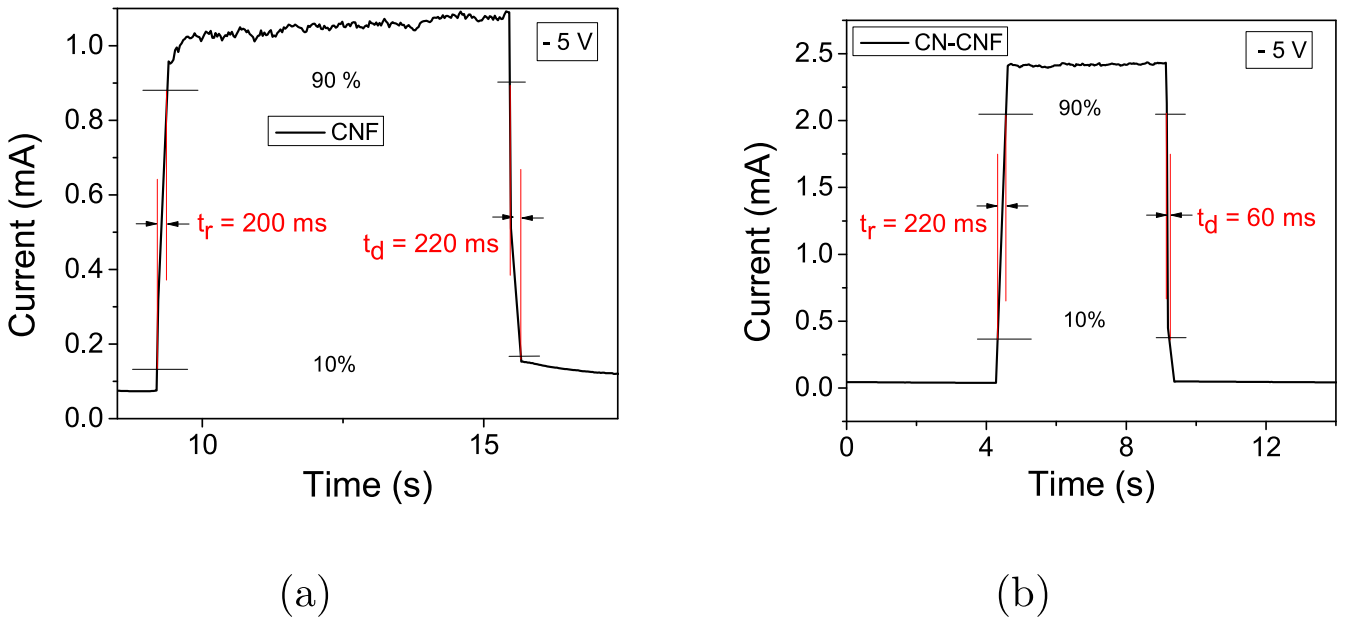

Figure 10. Photocurrent versus time curves of (a) CNF/Si and (b) CN-CNF/Si devices, showing the response and decay times.

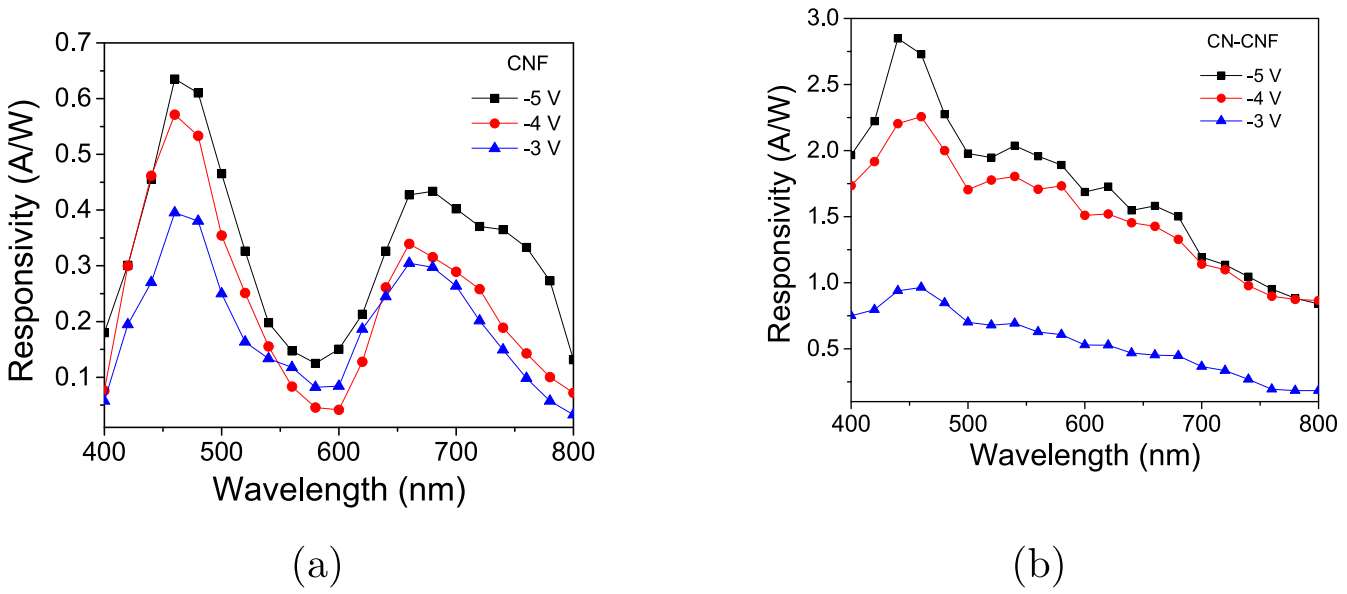

Figure 11. Spectral responsivities of (a) CNF/Si and (b) CN-CNF/Si devices under different reverse bias voltages.

$$R(\lambda) = J(\lambda)/P(\lambda) \quad (1)$$

with $J = I/A_D$ being the photocurrent density determined using the photocurrent I and the device area A_D, and P being the incident optical power density; (ii) the detectivity D, that measures the capacity of the photodetector to detect weak output signals and is estimated using[14,69−73]

$$D(\lambda) = \frac{R(\lambda) \times A_D^{1/2}}{(2qI_d)^{1/2}} \quad (2)$$

and (iii) the gain G, a measure of the number of generated electrons per photon and given by[74−78]

$$G = R\frac{h \cdot c}{q \cdot \lambda} \quad (3)$$

where q, h, and c are the electronic charge, Planck constant, and light speed, respectively. The formula used here for D is based on the assumption that the dominant contribution to the detector noise comes from the shot noise, which is parametrized in I_d. It is to be noted that an accurate description of D must include contributions also from various other noises, like Johnson noise, 1/f noise, generation-recombination noise, and electrical noise from the circuit.[79] However, based on several reports of use of eq 2, including that by Zhang et al.[14] for a similar magnitude of dark current, the use of I_d in estimating D has been followed in this work.

Spectral variations in the responsivities of the two devices were recorded under different reverse bias conditions. Figure 11a shows the R spectra of the CNF/Si device. According to the figure, the device shows a broadband photoresponse in the visible to near-infrared (400−800 nm) range. In general, the

https://doi.org/10.1021/acsomega.4c01546
ACS Omega 2024, 9, 27232−27247

Table 1. Comparison of Device Performance with Other Carbon Based Photodetectors[a]

device	λ (nm)	bias (V)	R (A/W)	D (Jones)	G	τ_r (ms)	τ_d (ms)	ref.
CN-CNF/Si	450	−5	2.8	9.4×10^9	8	200	220	this work
CNF/Si	450	−5	0.6	1.3×10^9	1.6	220	60	this work
CNTF/SLG/SiO_2	920	−3	0.2	4.87×10^{10}	0.43	0.07	0.08	14
MWCNT/Si	800	−9	0.32	3×10^{12}	0.65	3×10^{-5}		15
CNT/Si	950	−14	0.37		0.5		83	
Bi_2O_3-MWCNT/Si	560	−6.5	1.37	8.5×10^{11}	3			84
SWCNT/Si	650	−24	0.09			500		2
CNT/Si	950	−14	∼0.9		∼0.9			85
MWCNT-PANI/ITO	380	−3	0.009	12×10^{15}	0.32	350	330	86
CNT/Si-waveguide	1550	−2	0.073					4
CNT/Quartz	2000	−0.5	0.62		0.4			3
CNT/SiO_2/Si	1550	−1.5	1.5					5

[a] λ is the wavelength at which the responsivity (R) and detectivity (D) are a maximum. τ_r and τ_d are the response and decay times, respectively, of the photodetector.

responsivity increases with an increasing reverse bias. This bias dependence of responsivity comes via the known bias dependence of photocurrent from photodetectors.[80] Further, the spectra are divisible into two distinct response regions: (i) 400−600 nm, with a maximum responsivity of 0.6 A/W at 450 nm at a −5 V bias, and (ii) 600−800 nm, with another maximum responsivity of 0.4 A/W at 650 nm at the same bias. The enhanced responsivities in the 600−800 nm region are likely to arise due to the absorption edge of the silicon substrate.[15] The midrange minima (0.1 to 0.3 A/W) in the spectra are also considerably moderate and match well with previous reports.[17,19] The maximum responsivity is higher than the previously reported values for CNT/Si heterojunction photodetectors.[1,15,17] This itself suggests that CNF-based photodetectors have the potential to show a better photoresponse than CNT-based photodetectors.

The computed maximum values of D and G at 450 nm under a −5 V bias are 1.3×10^9 Jones and 1.6, respectively. The plots of D versus wavelength and G versus wavelength are demonstrated in Figures S1 and S2 of the Supporting Information. The maximum detectivity is moderate, while the maximum G value is quite high. For the high G value, the following mechanism is proposed: As mentioned earlier, CNF is a relatively high-defect material, e.g., compared to the nearest C allotrope CNT. This will lead to the formation of defect induced midgap states.[81] Immediately after photogeneration, the charge carriers relax to these additional states. This enhances the lifetime of the carriers and, thereby, reduces the chances of carrier recombination.[82] The trapped carriers are then also available later for the electrical conduction, leading to a high R, and hence high G of 1.6, of the CNF/n-Si device.

The bias-dependent spectral responsivity of the CN-CNF/Si device is shown in Figure 11b. As for the CNF/Si device, the spectral response is broadband and bias dependent, and the spectra exhibit a peak at 450 nm for all bias voltages. The other substrate-originated peak observable at 650 nm for the CNF/Si device appears as a broad hump over a gradual tapering beyond 500 nm in the case of the CN-CNF device. The maximum responsivity is 2.8 A/W at −5 V bias, which is higher than that of the CNF/Si device. The calculated corresponding (maximum) detectivity and G for the CN-CNF device are 9.4×10^9 Jones and 8, respectively, at 450 nm. The variation of D and G with wavelength is shown in Figures S3 and S4 of the Supporting Information, respectively. Thus, the CN-CNF/Si device is superior to the CNF/Si device. Adsorption of CuNi NPs on CNF, along with the charge transfer between the two, is expected to increase the number of midgap defect states further[25] and therefore raise the G value to the observed 8 level for the CN-CNF/n-Si device. The trap states are also responsible for the observed large dark current on the order of microamperes. A comparative plot of G versus wavelength for CN-CNF and CNF devices is depicted in Figure S5 of the Supporting Information.

The obtained values of R, D, and G for the CNF/Si and CN-CNF/Si devices are compared with these values for other reported C-based devices in Table 1.[2−5,14,15,83−86] As can be inferred, the responsivity and G, and hence the photoresponse of the presently studied devices, are much better than the earlier reported devices. The detectivities are also acceptably moderate for these devices to be used as photodetectors, although the performances overall are much inferior to the best photodetection performances reported in the literature.

The mechanism behind the observed photoresponses of the two devices can be understood with the help of the respective band diagrams, which, in turn, can be drawn using the corresponding energy level diagrams. The energy level diagram (derived using the values of valence band maximum from the corresponding VBXPS spectrum and work function from the literature[1,55]) for the p-CNF/n-Si device is shown in Figure 6e. The corresponding band diagram after zero biasing the device is shown in Figure 7b. For this zero bias, the estimated built-in potential is 1.11 V. In the absence of light (i.e., under dark conditions), essentially the thermally generated carriers are responsible for the (low) photocurrent (Figure 7a).[87] Illumination of the junction with light produces a large amount of photogenerated electron−hole (e-h) pairs, enhancing the photocurrent by an order of magnitude (Figure 7a).[88] Increasing the reverse bias increases the built-in potential and the depletion width, providing more photogenerated e-h pairs for making up the current. This results in an increased carrier collection rate and hence a further enhanced photocurrent with increasing bias (Figure 7a).[88] The energy level diagram for the p-CN-CNF/n-Si device, as derived using the corresponding VBXPS spectrum, is shown in Figure 6g. In this case, ϕ has increased (from 4.95 eV for CNF) to 5.55 eV. Further, the heterojunction formed is once a G of the desirable type II. According to the band diagram (Figure 7d) derived from the energy level diagram, the built-in potential in this case increases to 2.02 V. The increased built-in potential, as discussed earlier, results in the observed enhanced photo-

https://doi.org/10.1021/acsomega.4c01546
ACS Omega 2024, 9, 27232−27247

response of the p-CN-CNF/n-Si device over the p-CNF/n-Si device.

Finally, cycling tests of both the devices were performed for 20 on/off cycles under laser illumination at −2 V. The cyclic test result for the CN-CNF/Si device is shown in Figure S6 of the Supporting Information. The photocurrents are found to be quite stable throughout the 20 cycles. The variation of photocurrent versus the number of light cycles is depicted in Figure S7 of the Supporting Information. This reveals good retentivity of the device(s) after repeated on/off cycles.

CONCLUSIONS

The photodetection properties of a carbon nanofiber (CNF)-based CNF/Si heterostructure device in the visible to IR range and any change in these properties on adhesion of CuNi (CN) nanoparticles to the CNF layer have been investigated. The nanoparticles and CN-CNF composites were synthesized by using chemical hydrothermal methods. The CNFs and CN-CNF nanocomposites were then spin-coated onto n-Si substrates to fabricate the CNF/Si and CN-CNF/Si devices. From the TEM images, the nanoparticles are seen to be adsorbed on the CNF surfaces. Peak shifts in the XPS and Raman spectra suggest charge (electron) transfer from the adsorbates to the CNFs. UV−vis and valence band XPS spectra establish that the CNFs and CN-CNF composites were p-type semiconductors. The peak responsivity (0.6 A/W) and the G (1.6) of this device are found to be better than many CNT-based devices reported in the literature. The peak detectivity (1.3×10^9 Jones) of the device is also acceptably moderate. Further, the performance of the CN-CNF/Si device is superior to that of the CNF/Si device in that it has a better peak responsivity of 2.8 A/W, a peak detectivity of 9.4×10^9 Jones, and a G of 8. The enhancements are attributable to the charge transfer induced increase in the work function on adsorbing the CN nanoparticles onto the CNF surface, leading thereby to an increase in the junction built-in potential. It is proposed that the high G values are due to the trapping of charge carriers in defect induced midgap states, which must be present naturally in CNF and get enhanced in number on CuNi NP adsorption.

ASSOCIATED CONTENT

Supporting Information

The Supporting Information is available free of charge at https://pubs.acs.org/doi/10.1021/acsomega.4c01546.

Detectivity plots and G plots for CNF/Si and CN-CNF/Si devices; plots of photocurrent with time (cyclic stability test); and plots of photocurrent versus the number of light cycles (PDF)

AUTHOR INFORMATION

Corresponding Author

Sanjeev K. Srivastava − *Department of Physics, Indian Institute of Technology Kharagpur, Kharagpur WB - 721302, India;* orcid.org/0000-0001-9611-1001; Email: sanjeev@phy.iitkgp.ac.in

Authors

Shivam Shukla − *Department of Physics, Indian Institute of Technology Kharagpur, Kharagpur WB - 721302, India*

Subhajit Jana − *Department of Physics, Indian Institute of Technology Kharagpur, Kharagpur WB - 721302, India;* orcid.org/0000-0001-7832-3721

Anu Gupta − *Department of Chemical and Biological Physics, Weizmann Institute of Science, Rehovot 7610001, Israel*

Subhadip Ghosh − *Department of Physics, Indian Institute of Technology Kharagpur, Kharagpur WB - 721302, India*

Samit K. Ray − *Department of Physics, Indian Institute of Technology Kharagpur, Kharagpur WB - 721302, India;* orcid.org/0000-0002-8099-6690

Complete contact information is available at: https://pubs.acs.org/10.1021/acsomega.4c01546

Notes

The authors declare no competing financial interest.

ACKNOWLEDGMENTS

S.S. acknowledges IIT Kharagpur for providing the financial assistance to carry out this research work. We further acknowledge Suneel K. Srivastava for providing the CNF powder.

REFERENCES

(1) Zhao, Y.-M.; Hu, X.-G.; Shi, C.; Ding, W.-T.; Hou, P.-X.; Liu, C.; Cheng, H.-M. A high-performance photodetector based on small-bundled single-wall carbon nanotube film/silicon heterojunctions. *Journal of Materials Chemistry A* **2022**, *10*, 16986−16994.

(2) Capista, D.; Lozzi, L.; Di Bartolomeo, A.; Giubileo, F.; Martucciello, N.; Passacantando, M. SWCNT-Si photodetector with voltage-dependent active surface. *Nano Express* **2024**, *5*, 015004.

(3) Wu, W.; Ma, H.; Cai, X.; Han, B.; Li, Y.; Xu, K.; Lin, H.; Zhang, F.; Chen, Z.; Zhang, Z.; Peng, L.-M.; Wang, S. High-speed carbon nanotube photodetectors for 2 μm communications. *ACS Nano* **2023**, *17*, 15155−15164.

(4) Zhao, H.; Yang, L.; Wu, W.; Cai, X.; Yang, F.; Xiu, H.; Wang, Y.; Zhang, Q.; Xin, X.; Zhang, F.; Peng, L.-M.; Wang, S. Silicon waveguide-integrated carbon nanotube photodetector with low dark current and 48 GHz bandwidth. *ACS Nano* **2023**, *17*, 7466−7474.

(5) Wu, W.; Yang, F.; Fang, X.; Cai, X.; Liu, X.; Zhang, F.; Wang, S. Ultrafast Carbon Nanotube Photodetectors with Bandwidth over 60 GHz. *ACS Photonics* **2023**, *10*, 1060−1069.

(6) Dang, Q.; Hu, L.; Yuan, L.; Miao, X.; Huang, A.; Su, J.; Wang, J.; Zhou, Y.; Chen, X.; Li, Q.; Li, Z.; Deng, X. Enhanced gain in organic photodetectors using the polymer with singlet open-shell ground state. *Angew. Chem.* **2023**, *135*, No. e202312538.

(7) Zeng, L.; Wu, D.; Jie, J.; Ren, X.; Hu, X.; Lau, S. P.; Chai, Y.; Tsang, Y. H. Van der Waals epitaxial growth of mosaic-like 2D platinum ditelluride layers for room-temperature mid-infrared photodetection up to 10.6 μm. *Adv. Mater.* **2020**, *32*, 2004412.

(8) Zeng, L.-H.; Lin, S.-H.; Li, Z.-J.; Zhang, Z.-X.; Zhang, T.-F.; Xie, C.; Mak, C.-H.; Chai, Y.; Lau, S. P.; Luo, L.-B.; Tsang, Y. H. Fast, self-driven, air-stable, and broadband photodetector based on vertically aligned $PtSe_2$/GaAs heterojunction. *Adv. Funct. Mater.* **2018**, *28*, 1705970.

(9) Zeng, L.-H.; Wu, D.; Lin, S.-H.; Xie, C.; Yuan, H.-Y.; Lu, W.; Lau, S. P.; Chai, Y.; Luo, L.-B.; Li, Z.-J.; Tsang, Y. H. Controlled synthesis of 2D palladium diselenide for sensitive photodetector applications. *Adv. Funct. Mater.* **2019**, *29*, 1806878.

(10) Chen, H.; Zhu, J.; Cao, Y.; Wei, J.; Lv, B.; Hu, Q.; Sun, J.-l. Significantly enhanced photoresponse of carbon nanotube films modified with cesium tungsten bronze nanoclusters in the visible to short-wave infrared range. *RSC Adv.* **2021**, *11*, 39646−39656.

(11) Liu, Y.; Yin, J.; Wang, P.; Hu, Q.; Wang, Y.; Xie, Y.; Zhao, Z.; Dong, Z.; Zhu, J.-L.; Chu, W.; Yang, N.; Wei, J.; Ma, W.; Sun, J.-L. High-performance, ultra-broadband, ultraviolet to terahertz photo-

detectors based on suspended carbon nanotube films. *ACS Appl. Mater. Interfaces* **2018**, *10*, 36304−36311.
(12) Avouris, P.; Freitag, M.; Perebeinos, V. Carbon-nanotube photonics and optoelectronics. *Nat. Photonics* **2008**, *2*, 341−350.
(13) Zhou, X.; Liu, B.; Chen, Y.; Guo, L.; Wei, G. Carbon nanofiber-based three-dimensional nanomaterials for energy and environmental applications. *Materials Advances* **2020**, *1*, 2163−2181.
(14) Zhang, T.-F.; Li, Z.-P.; Wang, J.-Z.; Kong, W.-Y.; Wu, G.-A.; Zheng, Y.-Z.; Zhao, Y.-W.; Yao, E.-X.; Zhuang, N.-X.; Luo, L.-B. Broadband photodetector based on carbon nanotube thin film/single layer graphene Schottky junction. *Sci. Rep.* **2016**, *6*, 38569.
(15) Ismail, R. A.; Mohammed, M. I.; Mahmood, L. H. Preparation of multi-walled carbon nanotubes/n-Si heterojunction photodetector by arc discharge technique. *Optik* **2018**, *164*, 395−401.
(16) Kumar, R.; Khan, M. A.; Anupama, A.; Krupanidhi, S. B.; Sahoo, B. Infrared photodetectors based on multiwalled carbon nanotubes: Insights into the effect of nitrogen doping. *Appl. Surf. Sci.* **2021**, *538*, 148187.
(17) Huo, T.; Yin, H.; Zhou, D.; Sun, L.; Tian, T.; Wei, H.; Hu, N.; Yang, Z.; Zhang, Y.; Su, Y. Self-powered broadband photodetector based on single-walled carbon nanotube/GaAs heterojunctions. *ACS Sustainable Chem. Eng.* **2020**, *8*, 15532−15539.
(18) Scarselli, M.; Camilli, L.; Matthes, L.; Pulci, O.; Castrucci, P.; Gatto, E.; Venanzi, M.; De Crescenzi, M. Photoresponse from noble metal nanoparticles-multi walled carbon nanotube composites. *Appl. Phys. Lett.* **2012**, *101*, 241113.
(19) Qi, T.; Yu, Y.; Liu, J.; Jia, Y.; Ding, D. Enhanced performance of single-walled carbon nanotube-germanium near-infrared photodetector by doping with Au nanoparticles. *Photonics* **2022**, *9*, 615.
(20) Wang, Z.; Wu, S.; Wang, J.; Yu, A.; Wei, G. Carbon nanofiber-based functional nanomaterials for sensor applications. *Nanomaterials* **2019**, *9*, 1045.
(21) Baddorf, A. P.; Rondinone, A. J.; Hensley, D. K. Work function measurements of clean and modified carbon nanospikes. *Carbon* **2020**, *168*, 302−307.
(22) Sharon, M. In *Carbon Nanofibers: Fundamentals and Applications*; Sharon, M., Sharon, M., Eds.; Wiley Online Library, 2021; Chapter 1, pp 1−20.
(23) Shi, Q.; Wang, Y.; Wang, Z.; Lei, Y.; Wang, B.; Wu, N.; Han, C.; Xie, S.; Gou, Y. Three-dimensional (3D) interconnected networks fabricated via in-situ growth of N-doped graphene/carbon nanotubes on Co-containing carbon nanofibers for enhanced oxygen reduction. *Nano Research* **2016**, *9*, 317−328.
(24) Li, X.; Jia, Y.; Cao, A. Tailored single-walled carbon nanotube-CdS nanoparticle hybrids for tunable optoelectronic devices. *ACS Nano* **2010**, *4*, 506−512.
(25) Shukla, V.; Nandi, P.; Srivastava, S. K. Charge transfer, electronic transport and magnetic properties of $Cu_{1-x}Ni_x$/reduced graphene oxide nanocomposites. *Carbon* **2023**, *212*, 118102.
(26) Wei, J.; Geng, S.; Kumar, M.; Pitkänen, O.; Hietala, M.; Oksman, K. Investigation of structure and chemical composition of carbon nanofibers developed from renewable precursor. *Frontiers in Materials* **2019**, *6*, 334.
(27) mp-704645: CuO. https://next-gen.materialsproject.org/materials/mp-704645?formula=CuO.
(28) mp-19009: NiO. https://next-gen.materialsproject.org/materials/mp-19009?formula=NiO.
(29) Ravindra, R.; Badekai Ramachandra, B. High yield synthesis of carbon nanofibers in an environmental friendly route. *Applied Nanoscience* **2011**, *1*, 103−108.
(30) Albetran, H. M. Synthesis and characterization of electrospun carbon nanofibers from polyacrylonitrile and graphite nanoplatelets. *Materials* **2023**, *16*, 1749.
(31) Atomic form factors. http://lampx.tugraz.at/~hadley/ss1/crystaldiffraction/atomicformfactors/formfactors.php.
(32) mp-27912: $Ni(HO)_2$. https://next-gen.materialsproject.org/materials/mp-27912?formula=Ni292.
(33) mp-505105: $Cu(HO)_2$. https://next-gen.materialsproject.org/materials/mp-505105?formula=Cu(HO)2.
(34) Wu, P.; Yu, S.; Liu, H.; Zhang, X.; Hou, L.; Niu, B.; Jiang, J.; Liu, S.; Fu, J. Nickel−copper alloy nanoparticles embedded in N-doped porous carbon nanosheets for supercapacitors and hydrogen evolution reaction. *ACS Applied Nano Materials* **2022**, *5*, 9447−9459.
(35) Varga, M.; Izak, T.; Vretenar, V.; Kozak, H.; Holovsky, J.; Artemenko, A.; Hulman, M.; Skakalova, V.; Lee, D. S.; Kromka, A. Diamond/carbon nanotube composites: Raman, FTIR and XPS spectroscopic studies. *Carbon* **2017**, *111*, 54−61.
(36) Casillas-Trujillo, L.; Osinger, B.; Lindblad, R.; Karlsson, D.; Abrikosov, A. I.; Fritze, S.; von Fieandt, K.; Alling, B.; Hotz, I.; Jansson, U.; Abrikosov, I. A.; Lewin, E. Experimental and theoretical evidence of charge transfer in multi-component alloys − how chemical interactions reduce atomic size mismatch. *Mater. Chem. Front.* **2021**, *5*, 5746−5759.
(37) Bhattacharya, S.; Choi, W.; Ghosh, A.; Lee, S.; Lee, G.-D.; Kim, S.-K. Charge-transfer-induced 2D ferromagnetism and realization of thermo-remnant memory effect in ultrathin ß-NiOOH-encapsulated graphene. *Nanotechnology* **2021**, *32*, 385705.
(38) Sun, L.; Deng, Y.; Yang, Y.; Xu, Z.; Xie, K.; Liao, L. Preparation and catalytic activity of magnetic bimetallic nickel/copper nanowires. *RSC Adv.* **2017**, *7*, 17781−17787.
(39) Zhang, Z.; Deng, X.; Sunarso, J.; Cai, R.; Chu, S.; Miao, J.; Zhou, W.; Shao, Z. Two-step fabrication of $Li_4Ti_5O_{12}$-coated carbon nanofibers as a flexible film electrode for high-power lithium-ion batteries. *ChemElectroChem.* **2017**, *4*, 2286−2292.
(40) De Oliveira, J. B.; Guerrini, L. M.; Oishi, S. S.; de Oliveira Hein, L. R.; dos Santos Conejo, L.; Rezende, M. C.; Botelho, E. C. Carbon nanofibers obtained from electrospinning process. *Materials Research Express* **2018**, *5*, 025602.
(41) Chen, S.; Brown, L.; Levendorf, M.; Cai, W.; Ju, S.-Y.; Edgeworth, J.; Li, X.; Magnuson, C. W.; Velamakanni, A.; Piner, R. D.; Kang, J.; Park, J.; Ruoff, R. S. Oxidation resistance of graphene-coated Cu and Cu/Ni alloy. *ACS Nano* **2011**, *5*, 1321−1327.
(42) Deng, Y.; Handoko, A. D.; Du, Y.; Xi, S.; Yeo, B. S. In situ Raman spectroscopy of copper and copper oxide surfaces during electrochemical oxygen evolution reaction: identification of CuIII oxides as catalytically active species. *ACS Catal.* **2016**, *6*, 2473−2481.
(43) Bala, N.; Singh, H. K.; Verma, S.; Rath, S. Magnetic-order induced effects in nanocrystalline NiO probed by Raman spectroscopy. *Phys. Rev. B* **2020**, *102*, 024423.
(44) Zhang, C.-F.; Huang, Z.-B.; Yan, X.-W.; Lin, H.-Q. Charge transfer effect on Raman shifts of aromatic hydrocarbons with three phenyl rings from ab initio study. *J. Chem. Phys.* **2019**, *150*, 074306.
(45) Cirera, B.; Litman, Y.; Lin, C.; Akkoush, A.; Hammud, A.; Wolf, M.; Rossi, M.; Kumagai, T. Charge transfer-mediated dramatic enhancement of Raman scattering upon molecular point contact formation. *Nano Lett.* **2022**, *22*, 2170−2176.
(46) Rao, R.; Pierce, N.; Dasgupta, A. On the charge transfer between single-walled carbon nanotubes and graphene. *Appl. Phys. Lett.* **2014**, *105*, 073115.
(47) Gupta, V. In *Principles and Applications of Quantum Chemistry*; Gupta, V., Ed.; Academic Press: Boston, 2016; pp 385−433.
(48) Electronegativities of the elements (data page). https://en.wikipedia.org/wiki/Electronegativities_of_the_elements_(data_page).
(49) Hashim, U.; Farehanim, M. A.; Azizah, N.; Norhafiezah, S.; Fatin, M. F.; Ruslinda, A. R.; Ayub, R. M. Optical properties of MWCNTs dispersed in various solutions. *2015 2nd International Conference on Biomedical Engineering (ICoBE)*; IEEE, 2015; pp 1−3.
(50) Moumen, A.; Fattouhi, M.; Abderrafi, K.; El Hafidi, M.; Ouaskit, S. Nickel colloid nanoparticles: synthesis, characterization, and magnetic properties. *Journal of Cluster Science* **2019**, *30*, 581−588.
(51) El-Khatib, A. M.; Badawi, M. S.; Roston, G. D.; Moussa, R. M.; Mohamed, M. M. Structural and magnetic properties of nickel nanoparticles prepared by arc discharge method using an ultrasonic nebulizer. *Journal of Cluster Science* **2018**, *29*, 1321−1327.
(52) Rahman, L.-u.; Shah, A.; Lunsford, S. K.; Han, C.; Nadagouda, M. N.; Sahle-Demessie, E.; Qureshi, R.; Khan, M. S.; Kraatz, H.-B.; Dionysiou, D. D. Monitoring of 2-butanone using a Ag−Cu bimetallic

https://doi.org/10.1021/acsomega.4c01546
ACS Omega 2024, 9, 27232−27247

alloy nanoscale electrochemical sensor. *RSC Adv.* **2015**, *5*, 44427−44434.
(53) Makuła, P.; Pacia, M.; Macyk, W. How to correctly determine the band gap energy of modified semiconductor photocatalysts based on UV−vis spectra. *J. Phys. Chem. Lett.* **2018**, *9*, 6814−6817.
(54) Dincer, K.; Waisi, B.; Önal, G.; Tuğluoğlu, N.; McCutcheon, J.; Yüksel, Ö. Investigation of optical and dispersion parameters of electrospinning grown activated carbon nanofiber (ACNF) layer. *Synth. Met.* **2018**, *237*, 16−22.
(55) Shiraishi, M.; Ata, M. Work function of carbon nanotubes. *Carbon* **2001**, *39*, 1913−1917.
(56) Hu, W.; Yang, J. Two-dimensional Van der Waals heterojunctions for functional materials and devices. *J. Mater. Chem. C* **2017**, *5*, 12289−12297.
(57) Zhou, Y. H.; Zhang, Z. B.; Xu, P.; Zhang, H.; Wang, B. UV-visible photodetector based on I-type heterostructure of ZnO-QDs/monolayer MoS_2. *Nanoscale Res. Lett.* **2019**, *14*, 364.
(58) Gupta, A.; Chowdhury, R. K.; Ray, S.; Srivastava, S. Selective photoresponse of plasmonic silver nanoparticle decorated Bi_2Se_3 nanosheets. *Nanotechnology* **2019**, *30*, 435204.
(59) Kaja, K. Development of nano-probe techniques for work function assessment and application to materials for microelectronics. Université Joseph-Fourier Grenoble I, 2010. https://theses.hal.science/tel-00515370/preview/K-KAJA_Thesis.PDF.
(60) Moran-Lopez, J.; Bosch, A. Changes in work function due to charge transfer in chemisorbed layers. *Surf. Sci.* **1977**, *68*, 377−384.
(61) Gossenberger, F.; Roman, T.; Forster-Tonigold, K.; Groß, A. Change of the work function of platinum electrodes induced by halide adsorption. *Beilstein J. Nanotechnol.* **2014**, *5*, 152−161.
(62) de Andrade, A. M.; Kullgren, J.; Broqvist, P. Controlling the metal work function through atomic-scale surface engineering. *Appl. Surf. Sci.* **2022**, *589*, 152932.
(63) Leung, T. C.; Kao, C. L.; Su, W. S.; Feng, Y. J.; Chan, C. T. Relationship between surface dipole, work function and charge transfer: Some exceptions to an established rule. *Phys. Rev. B* **2003**, *68*, 195408.
(64) Pansri, S.; Supruangnet, R.; Nakajima, H.; Rattanasuporn, S.; Noothongkaew, S. Band offset determination of p-NiO/n-TiO_2 heterojunctions for applications in high-performance UV photodetectors. *J. Mater. Sci.* **2020**, *55*, 4332−4344.
(65) Simone, G.; Dyson, M. J.; Weijtens, C. H. L.; Meskers, S. C. J.; Coehoorn, R.; Janssen, R. A. J.; Gelinck, G. H. On the origin of dark current in organic photodiodes. *Advanced Optical Materials* **2020**, *8*, 1901568.
(66) Shao, D.; Yu, M.; Lian, J.; Sawyer, S. Heterojunction photodiode fabricated from multiwalled carbon nanotube/ZnO nanowire/p-silicon composite structure. *Appl. Phys. Lett.* **2013**, *102*, 021107.
(67) Kumar, A.; Husale, S.; Srivastava, A.; Dutta, P.; Dhar, A. Cu−Ni nanoparticle-decorated graphene based photodetector. *Nanoscale* **2014**, *6*, 8192−8198.
(68) Mao, J.; Yu, Y.; Wang, L.; Zhang, X.; Wang, Y.; Shao, Z.; Jie, J. Ultrafast, broadband photodetector based on $MoSe_2$/silicon heterojunction with vertically standing layered structure using graphene as transparent electrode. *Advanced Science* **2016**, *3*, 1600018.
(69) Mukherjee, S.; Chowdhury, R. K.; Karmakar, D.; Wan, M.; Jacob, C.; Das, S.; Ray, S. K. Plasmon triggered, enhanced light−matter interactions in Au−MoS_2 coupled system with superior photosensitivity. *J. Phys. Chem. C* **2021**, *125*, 11023−11034.
(70) Zhu, Y.; Yang, T.; Ding, H.; Lin, G.; Li, C.; Huang, W.; Chen, S.; Wang, J.; Xu, J. Sputtering-grown undoped GeSn/Ge multiple quantum wells on n-Ge for low-cost visible/shortwave infrared dual-band photodetection. *Appl. Surf. Sci.* **2024**, *656*, 159673.
(71) Zhang, Q.; Li, Q.; Chen, R.; Zhang, M.; Fang, W.; Li, J.; Wang, M.; Yun, F.; Wang, T.; Hao, Y. Large-area self-assembled hexagonal boron nitride nanosheet films for ultralow dark current vacuum-ultraviolet photodetectors. *Adv. Funct. Mater.* **2024**, 2315149.
(72) Yao, L.; Ji, R.; Wu, S.; Jiao, J.; He, F.; Wang, D.; Wang, J.; Li, C.; Huang, W.; Ke, S.; Lin, G.; Chen, S. Low dark current lateral Ge PIN photodetector array with resonant cavity effect for short wave infrared imaging. *J. Phys. D: Appl. Phys.* **2024**, *57*, 165103.
(73) Chen, Z.; Huang, T.; Zhang, B.; Wu, C.; Zhang, X.; Sun, T.; Xu, W.; Kang, K.; Xiang, C.; Zhang, T.; Li, R. Suppression of the dark current in PbS quantum dot infrared photodetectors through the introduction of a CuInSeS interfacial layer. *Journal of Materials Chemistry C* **2024**, *12*, 4493−4500.
(74) Wu, D.; Xu, M.; Zeng, L.; Shi, Z.; Tian, Y.; Li, X. J.; Shan, C.-X.; Jie, J. In situ fabrication of $PdSe_2$/GaN schottky junction for polarization-sensitive ultraviolet photodetection with high dichroic ratio. *ACS Nano* **2022**, *16*, 5545−5555.
(75) Wu, D.; Guo, J.; Wang, C.; Ren, X.; Chen, Y.; Lin, P.; Zeng, L.; Shi, Z.; Li, X. J.; Shan, C.-X.; Jie, J. Ultrabroadband and high-detectivity photodetector based on WS_2/Ge heterojunction through defect engineering and interface passivation. *ACS Nano* **2021**, *15*, 10119−10129.
(76) Wu, D.; Guo, J.; Du, J.; Xia, C.; Zeng, L.; Tian, Y.; Shi, Z.; Tian, Y.; Li, X. J.; Tsang, Y. H.; Jie, J. Highly polarization-sensitive, broadband, self-powered photodetector based on graphene/$PdSe_2$/germanium heterojunction. *ACS Nano* **2019**, *13*, 9907−9917.
(77) Wu, D.; Guo, C.; Zeng, L.; Ren, X.; Shi, Z.; Wen, L.; Chen, Q.; Zhang, M.; Li, X. J.; Shan, C.-X.; Jie, J. Phase-controlled Van der Waals growth of wafer-scale 2D $MoTe_2$ layers for integrated high-sensitivity broadband infrared photodetection. *Light: Science & Applications* **2023**, *12*, 5.
(78) Zeng, L.; Han, W.; Wu, S.-E.; Wu, D.; Lau, S. P.; Tsang, Y. H. Graphene/$PtSe_2$/pyramid Si Van der Waals schottky junction for room-temperature broadband infrared light detection. *IEEE Trans. Electron Devices* **2022**, *69*, 6212−6216.
(79) Zeng, L.; Han, W.; Ren, X.; Li, X.; Wu, D.; Liu, S.; Wang, H.; Lau, S. P.; Tsang, Y. H.; Shan, C.-X.; Jie, J. Uncooled mid-infrared sensing enabled by chip-integrated low-temperature-grown 2D $PdTe_2$ Dirac semimetal. *Nano Lett.* **2023**, *23*, 8241−8248.
(80) Tarr, N.; Pulfrey, D. An investigation of dark current and photocurrent superposition in photovoltaic devices. *Solid-State Electron.* **1979**, *22*, 265−270.
(81) Pujari, B. S.; Kanhere, D. G. Density functional investigations of defect-induced mid-gap states in graphane. *J. Phys. Chem. C* **2009**, *113*, 21063−21067.
(82) Bera, K. P.; Haider, G.; Usman, M.; Roy, P. K.; Lin, H.-I.; Liao, Y.-M.; Inbaraj, C. R. P.; Liou, Y.-R.; Kataria, M.; Lu, K.-L.; Chen, Y.-F. Trapped photons induced ultrahigh external quantum efficiency and photoresponsivity in hybrid graphene/metal-organic framework broadband wearable photodetectors. *Adv. Funct. Mater.* **2018**, *28*, 1804802.
(83) Pelella, A.; Capista, D.; Passacantando, M.; Faella, E.; Grillo, A.; Giubileo, F.; Martucciello, N.; Di Bartolomeo, A. A self-powered CNT−Si photodetector with tuneable photocurrent. *Advanced Electronic Materials* **2023**, *9*, 2200919.
(84) Shaker, S. S.; Ismail, R. A.; Ahmed, D. S. High-Responsivity heterojunction photodetector based on Bi_2O_3-decorated MWCNTs nanostructure grown on silicon via laser ablation in liquid. *Journal of Inorganic and Organometallic Polymers and Materials* **2022**, *32*, 1381−1388.
(85) Pelella, A.; Capista, D.; Grillo, A.; Faella, E.; Passacantando, M.; Martucciello, N.; Giubileo, F.; Romano, P.; Di Bartolomeo, A. Enhanced photodetection in carbon-based devices with MIS parallel structure. *2023 IEEE Nanotechnology Materials and Devices Conference (NMDC)*; IEEE, 2023; pp 214−217.
(86) Khudeir, H.; Hubeatir, K. A.; Umran, F. A. Developing a high-performance UV photodetector by improving polyaniline polymer properties with multi-walled carbon nanotubes. *Journal of Optics* **2024**, 1−11.
(87) Stiff-Roberts, A. In *Comprehensive Semiconductor Science and Technology*; Bhattacharya, P., Fornari, R., Kamimura, H., Eds.; Elsevier: Amsterdam, 2011; pp 452−485.
(88) Jana, S.; Mukherjee, S.; Bhaktha BN, S.; Ray, S. K. Plasmonic silver nanoparticle-mediated enhanced broadband photoresponse of

https://doi.org/10.1021/acsomega.4c01546
ACS Omega 2024, 9, 27232−27247

few-layer phosphorene/Si vertical heterojunctions. *ACS Appl. Mater. Interfaces* **2022**, *14*, 1699−1709.

https://doi.org/10.1021/acsomega.4c01546
ACS Omega 2024, 9, 27232−27247